Preferential oxidation of carbon monoxide in hydrogen using zinc oxide photocatalysts promoted and tuned by adsorbed copper ions

Yusuke Yoshida [a], Yu Mitani [a], Takaomi Itoi [b], Yasuo Izumi [a,*]

[a] Department of Chemistry, Graduate School of Science, Chiba University, Yayoi 1-33, Inage-ku, Chiba 263-8522, Japan
[b] Department of Mechanical Engineering, Graduate School of Engineering, Chiba University, Yayoi 1-33, Inage-ku, Chiba 263-8522, Japan

ARTICLE INFO

ABSTRACT

Preferential oxidation of CO (63 Pa) and O_2 (76 Pa) in H_2 (6.3 kPa) using spheroidal ZnO nanoparticles (22 nm × 47 nm) converted 52% of CO into CO_2, and selectivity to CO_2 was 92 mol% under UV–visible light for 5 h. When 0.5 wt.% of Cu^{2+} was adsorbed on ZnO, 91% of CO was converted into CO_2 with a selectivity of 99 mol% under UV–visible light for 3 h. CO (63 Pa) was photocatalytically decreased to 2.3 mPa (0.35 ppm) in O_2 (150 Pa) and H_2 (6.3 kPa) for 5 h with a selectivity of 94 mol%. As evident from a XANES peak at 8983.1 eV, the surface Cu^{II} sites trapped photogenerated electrons. Furthermore, O_2-derived species were reduced by accepting electrons from Cu^I and protons from the neighboring formate species, as indicated by the FT-IR peaks at 2985, 2879, 1627, 1587, and 1297 cm^{-1}.

1. Introduction

The production, storage, and transportation of hydrogen are key technologies for the emergence of a hydrogen energy society in the near future [1]. Fuel cells (FCs) as the key device to convert hydrogen into electricity for use in vehicles, mobile phones, and at home are indispensable for a hydrogen energy society. A significant part of the cost of FCs can be attributed to the electrode catalysts, which are mostly composed of Pt. However, electrode catalysts are easily deactivated if more than 10 ppm (under 1.0 Pa of ambient pressure) of CO is contained as an impurity in hydrogen because of the strong irreversible adsorption of CO on the Pt surface [2].

Well-known techniques for purifying hydrogen include pressure swing adsorption (PSA) [3], separation using metal membranes [4], cryogenic separation [4], and preferential oxidation (PROX) of CO [5–8]. PSA and metal membrane separation are advantageous for achieving higher hydrogen purity, whereas cryogenic separation recovers a larger amount of hydrogen gas. The apparatus of PSA incurs high initial investment costs and therefore is not appropriate for small-scale/personal use. Membrane separation typically uses Pd metal, whereas the PROX reaction of CO often utilizes expensive metals such as Au and Pt as the supported nanoparticle metal. To generate environmentally benign energy for small-scale/personal use, a new method for the purification of hydrogen that employs a cheap and sustainable membrane/catalyst is demanded.

For this purpose, the PROX reaction of CO using catalysts that do not contain noble metals and that can be excited under natural light is ideal. Such photo-PROX reactions of CO have been reported using an NiO/TiO_2 photocatalyst consisting of 0.5 wt.% NiO with a CO conversion of 89%, defined as the CO decrease ratio at 3 h, and a CO_2 selectivity of 98%, defined as the CO_2 formation divided by the H_2 decrease + CO_2 formation at 3 h [9], as well as a Mo/SiO_2 photocatalyst consisting of 0.6 wt.% Mo with a CO conversion of ~100% and a CO_2 selectivity of 99%. Both photocatalysts were tested in CO (3.8 μmol) + O_2 (7.5 μmol) + H_2 (24.6 μmol) illuminated by a high-pressure mercury lamp [10]. In particular, the Mo/SiO_2 photocatalyst reduced CO to less than 10 ppm in H_2. However, the mechanism of the reaction including the effects of the partial pressures of H_2 and O_2 and the factors that determine the selectivity of the photo-PROX reactions of CO are still debatable.

In this study, photo-PROX reactions were investigated using zinc oxide-based photocatalysts at 290 K. Nanoparticles/nanorods of ZnO with a narrow size distribution were synthesized, and their additive effects on the PROX reactions of CO were examined. The Cu–ZnO photocatalysts reduced 9700 ppm of CO to as small as 0.35 ppm in 5 h under UV–visible light. The effects of adsorbed Cu^{2+} were investigated using nitrogen gas adsorption, UV–visible absorption, X-ray diffraction (XRD), scanning electron microscopy (SEM), high-resolution transmission electron microscopy (TEM), Fourier-transform infrared absorption (FT-IR), and X-ray absorption fine structure (XAFS). The photo-PROX reaction mechanism is discussed herein.

* Corresponding author. Fax: +81 43 290 2783.
  E-mail address: yizumi@faculty.chiba-u.jp (Y. Izumi).

2. Experimental

2.1. Syntheses of ZnO

Spheroidal ZnO nanoparticles were synthesized according to a reported procedure [11]. Zn acetate dihydrate (11.6 g, 53 mmol; 99%, Wako Pure Chemical) was suspended in ethanol (110 mL). A 0.50 M sodium hydroxide ethanol solution (50 mL, 25 mmol; 97%, Kanto Chemical) was added to the Zn^{2+} solution over 20 min and was agitated using ultrasound (85 W, 28 kHz). The mixed suspension was refluxed at 353 K for 3 days. The obtained white precipitate was filtered using a polytetrafluoroethane-based membrane filter (Omnipore JGWP04700, Millipore) with a pore size of 0.2 μm, washed with deionized water, and dried at 333 K for 12 h.

Rod-like ZnO nanoparticles were synthesized according to a reported procedure [12]. A 0.20 M Zn sulfate heptahydrate aqueous solution (30 mL, 6.0 mmol; 99.5%, Kanto Chemical) was added to 1.33 M NaOH (90 mL, 120 mmol) over 6 min. The suspension was maintained at 333 K for 2 h. The white precipitate obtained was filtered using Omnipore JGWP04700, washed with deionized water, and dried at 333 K for 12 h. Commercial ZnO (FZO-50, ZnO 97.4 wt.%) was kindly provided by Ishihara Sangyo Co.

2.2. Syntheses of doped ZnO and Au–TiO₂

A 0.40 mM Cu nitrate trihydrate aqueous solution (30 mL; 99.9%, Wako Pure Chemical) was added to spheroidal ZnO (150 mg), which was synthesized as described in the previous section, and magnetically stirred at 290 K for 30 min. The obtained light blue powder was filtered using Omnipore JGWP04700, washed with deionized water, and dried at 333 K for 8 h. This compound is hereafter denoted as Cu–spheroidal ZnO. Most or all Cu ions introduced were adsorbed on ZnO, as confirmed by X-ray absorption spectra (see Section 2.3), and the Cu content was typically 0.5 wt.% and varied between 0.01 and 1.0 wt.%.

Furthermore, a 0.40 mM $Cu(NO_3)_2 \cdot 3H_2O$ aqueous solution (30 mL) was mixed with spheroidal ZnO (150 mg) and ethanol (1 mL) as a reductant. The suspension was stirred using a magnetic stirrer under the illumination of UV–visible light from a xenon arc lamp (Model UXL-500D-O, Ushio) set at 300 W for 1 h. The distance between the light exit window and the flask was 181 mm. The color of the suspended powder changed from light blue to yellow, suggesting the reduction of Cu^{II} sites to Cu^{I} during illumination. The yellow powder obtained was filtered using Omnipore JGWP04700 and treated via the same procedure used for Cu–spheroidal ZnO. This compound is hereafter denoted as Cu–spheroidal ZnO-reduced.

Spheroidal ZnO (150 mg) was suspended in a cerium nitrate hexahydrate aqueous solution (30 mL, 0.18 mM; >98%, Wako Pure Chemical) and stirred at 290 K for 30 min. The pale yellow powder was filtered using Omnipore JGWP04700, washed with deionized water (200 mL), and dried at 333 K for 8 h. This compound is henceforth denoted as Ce–spheroidal ZnO. Most or all Ce ions introduced were adsorbed on ZnO, as confirmed by X-ray absorption spectra, and the Ce content was 0.5 wt.%.

Zn acetate dihydrate (0.859 g, 3.91 mmol) was suspended in ethanol (10 mL) using ultrasound (85 W, 28 kHz) for 1 h. Ethanethiol (0.10 mL, 1.4 mmol; >98%, Wako Pure Chemical) was added to the suspension. The mixture was introduced into an autoclave (TVS-1-30, Taiatsu Techno) and maintained at 433 K for 24 h. The pale yellow powder obtained was filtered using Omnipore JGWP04700 and washed with ethanol (200 mL), deionized water (200 mL), and acetone (50 mL). The maximum S-content should be 12.4 wt.%, but the actual value was smaller because a notable smell originating from S remained in the initial portions of the solvents used for washing.

A reference Au–TiO₂ catalyst was prepared via the deposition–precipitation method [13,14]. 2.5 mM hydrogen tetrachloroaurate(III) tetrahydrate (100 mL; 99%, Wako Pure Chemical) was added over 1 h to TiO₂ (0.95 g; P25, Degussa; anatase/rutile phase = 7/3, specific surface area = 60 m² g⁻¹) and was suspended in a minimum amount of deionized water. Then, a 25 mM urea solution (100 mL) was added to the suspension over 90 min. The mixture was stirred at 353 K for 21 h in the absence of light. The powder obtained was filtered using a 1G glass filter (Shibata Scientific Technol.), washed with deionized water (total 150 mL), and dried at 353 K for 18 h. The light yellow-green powder obtained was calcined in air with an elevation rate of 4 K min⁻¹ and was maintained at 573 K for 4 h. The Au content in the purple powder finally obtained was 5.0 wt.%.

2.3. Characterization

N₂ adsorption isotherm measurements were performed at 77 K in the pressure range of 1.0–90 kPa in a vacuum system connected to diffusion and rotary pumps (10⁻⁶ Pa) and equipped with a capacitance manometer (Models CCMT-1000A and GM-2001, ULVAC). The Brunauer–Emmett–Teller (BET) surface area (S_{BET}) was calculated using eight-point measurements between 10 and 46 kPa (P/P_0 = 0.10–0.45) in the adsorption isotherm. The samples (100–200 mg) were evacuated, and the temperature was elevated at a rate of 5 K min⁻¹ to 393 K and maintained at 393 K for 2 h before the measurements.

XRD data for the sample powders were obtained using a MiniFlex diffractometer (Rigaku) at a Bragg angle (θ_B) of $2\theta_B$ = 10–80° with a scan step of 0.01° and a scan rate of 7 s/step. The measurements were performed at 30 kV and 15 mA using Cu Kα emission and a nickel filter. SEM measurements were performed using Hitachi Model S-80U. The samples were mounted on a conducting carbon tape. The electron accelerating voltage was 3.0 kV, and the magnification was between 2000 and 200,000 times. In addition, SEM images were observed using JEOL Model JSM-6510A at the Chemical Analysis Center, Chiba University. The electron accelerating voltage was in the range of 15–30 kV, and the magnification ranged from 2000 to 80,000 times. The samples were mounted on a conducting carbon tape (JEOL, DTM9101) and coated with gold.

High-resolution TEM measurements were performed using TEM equipment (JEOL, Model JEM-2010F) with an accelerating voltage of 200 kV. Samples were dispersed in ethanol (>99.5%) and mounted on amorphous C-coated Cu mesh (CU150 Mesh, JEOL).

Optical spectroscopic measurements were performed using a UV–visible spectrophotometer (JASCO, Model V-650). D₂ and halogen lamps were used for wavelengths below and above 340 nm, respectively, and an integrating sphere (JASCO, Model ISV-469) was used for diffuse reflectance measurements. Measurements were performed at 290 K in the wavelength range of 200–800 nm using fresh samples (100–200 mg). Diffuse reflectance spectra were converted to absorption spectra using the Kubelka–Munk equation [15,16]. The bandgap value was calculated by the simple extrapolation of the absorption edge or by fitting to the equation of Davis and Mott [15,16]:

$$\alpha \times h\nu \propto (h\nu - E_g)^n,$$

where α, h, and ν are the absorption coefficient, Planck's constant, and the wavenumber, respectively, and n is 1/2, 3/2, 2, and 3 for allowed direct, forbidden direct, allowed indirect, and forbidden indirect transitions, respectively.

FT-IR spectra were measured using a single-beam model FT/IR-4200 spectrophotometer (JASCO) in the wavenumber region between 4000 and 650 cm^{-1}. A MCT-M detector was used, and the energy resolution was set to 1–4 cm^{-1}. The sample was set as a disk (ϕ = 20 mm, 80–150 mg) in a quartz reactor equipped with NaCl windows on both sides and connected to a vacuum reaction system (10^{-6} Pa).

Cu K-edge XAFS spectra were measured at 290 K on a beamline 9C and 7C in the transmission mode in the Photon Factory at the High Energy Accelerator Research Organization (Tsukuba). The storage ring energy was 2.5 GeV, and the ring current was 450 mA. A Si(1 1 1) double-crystal monochromator was inserted in the X-ray beam path. The X-ray intensity was maintained at 65% of the maximum flux using a Piezo translator set on the crystal. The slit opening size in front of the I_0 ionization chamber was 1 mm (vertical) $\times$ (1–2) mm (horizontal). The I_0 and $I_{transmit}$ ionization chambers were purged with N$_2$ and Ar gases, respectively. Cu K-edge XAFS spectra were also measured at 290 K on a beamline 01B1 at SPring-8. The storage ring energy was 8 GeV, and the ring current was 100 mA. A Si(1 1 1) double-crystal monochromator and an Rh-coated double-mirror were inserted in the X-ray beam path. The incident angle of the X-ray to the mirror was set to 3.0 mrad.

The sample disk was set in a Pyrex glass cell equipped with a 25-μm-thick polyethylene naphthalate window (Q51-25, Teijin). The sample was vertically positioned at the center between the exit window of the I_0 ionization chamber and the entrance windows of the $I_{transmit}$ ionization chamber and tilted to make the X-ray incident angle to the sample surface equal to 45°. The sample was illuminated with an Xe arc lamp (500 W, UXL-500D-O) placed perpendicular to the X-ray beam path in the same horizontal plane with the initial pressures of CO (135 Pa), O$_2$ (270 Pa), and H$_2$ (13.1 kPa). The distance between the center of the sample and the exit window of the lamp house (Model UI-502Q) was 262 mm. The scan steps were ∼9, ∼0.3, and ∼2.5 eV in the pre-edge, edge, and post-edge regions, respectively. The data accumulation time was 0.5–1.0 s for each data point. The Cu K-edge absorption energy value was calibrated to 8980.3 eV for the spectrum of Cu metal [17,18]. The energy position of the monochromator was reproduced within ±0.1 eV.

The XAFS data were analyzed using an XDAP package [19]. The pre-edge background was approximated by the modified Victoreen function $C_2/E^2 + C_1/E + C_0$. The background of post-edge oscillation was approximated by a smoothing spline function calculated using the following equation for the number of data points, where k is the wavenumber of photoelectrons.

$$\sum_{i=1}^{\text{Data\_Points}} \frac{(\mu x_i - BG_i)^2}{\exp(-0.075 k_i^2)} \leqslant \text{smoothing factor}$$

2.4. PROX reaction of CO

The photo-PROX reactions of CO were performed in a closed circulating system (total volume: 143 mL) using a photoreaction quartz cell [20–22]. The catalyst (typically 50 mg, varied between 25 and 100 mg) was homogenously spread in the quartz reaction cell (bottom flat plate area: 23.8 cm^2) connected to the circulation loop and was evacuated (10^{-6} Pa) at 290 K for 2 h until the desorbed gas was detected by an online gas chromatograph (GC). H$_2$ (0.60–63 kPa, 0.035–3.7 mmol), CO (63 Pa, 3.7 μmol), and O$_2$ (76–150 Pa, 4.5–9.0 μmol) were introduced. In addition, a CO (63 Pa) oxidation test (O$_2$ 150 Pa) in the absence of H$_2$ was performed.

The catalyst in the quartz reactor was illuminated for 3–5 h with UV–visible light from the 500-W Xe arc lamp placed beneath the flat bottom. The distance between the bottom of the reactor and the lamp exit was set to 24 mm. The light intensity at the

wavelength of 555 nm was 42 mW cm^{-2} at the center of the sample cell and 28 mW cm^{-2} at the periphery of the bottom plate of the sample cell. Note that the intensity was measured at 555 nm, but the lamp irradiated in the wide spectrum of 200–1100 nm. During illumination, the temperature was 305 K at the catalyst position [20]. A sharp cutoff filter L-42 (>420 nm) was placed at the light exit to examine the photo-PROX reactions under visible light alone.

The products and reactants were analyzed using columns of Molecular Sieve 13X-S and polyethylene glycol (PEG)-6000 supported on Flusin P (GL Sciences) set in the online GC equipped with a thermal conductivity detector (Shimadzu, Model GC-8A). The changes in CO pressure during the photo-PROX reactions could be fit to the following first-order reaction equation:

$$-\frac{dP_{CO,t}}{dt} = kP_{CO,t}$$

$$P_{CO,t} = P_{CO,initial} e^{-kt}$$

Here, $P_{CO,initial}$ is the initial CO pressure and k is the rate constant. In some tests, the CO pressure converged to a certain value not equal to zero ($P_{CO,final}$) owing to the total consumption of O$_2$ gas during the tests, according to the following equation.

$$-\frac{dP_{CO,t}}{dt} = k(P_{CO,t} - P_{CO,final})$$

$$P_{CO,t} = P_{CO,final} + (P_{CO,initial} - P_{CO,final}) e^{-kt}$$

The changes in the CO pressure data during the photo-PROX reactions were also fit to the following 3/2 order reaction, but did not fit well for any test data.

$$-\frac{dP_{CO,t}}{dt} = k(P_{CO,t})^{\frac{3}{2}}$$

$$P_{CO,t} = \frac{1}{\left(\frac{1}{\sqrt{P_{CO,initial}}} + \frac{k}{2} t \right)^2}$$

Several blank tests were performed, including reaction tests under illumination with UV–visible or visible light alone in the absence of photocatalysts and reaction tests using Cu–spheroidal ZnO in the absence of reactants or in the absence of any light at 290 or 327 K. The reactor was in water bath controlled at 327 K in the latter test. For the test in the absence of light, the reactor was completely covered with a 20-μm-thick aluminum foil.

3. Results

3.1. Nitrogen adsorption, XRD, SEM, TEM, and UV–visible and FT-IR spectra

The S_{BET} value was measured on the basis of the N$_2$ adsorption of ZnO and the modified ZnO samples. The S_{BET} value for spheroidal ZnO was 35 m^2 g^{-1} and the value decreased to 57% for rod-like ZnO (Table 1a and b). The S_{BET} values for Cu–spheroidal ZnO and Ce–spheroidal ZnO increased by 11% and 26%, respectively, compared with that for spheroidal ZnO (Table 1c and d). Under the condition that the average particle size of 34–48 nm for the synthesized samples estimated on the basis of the XRD peak width was greater than 21 nm for FZO-50, the S_{BET} values for the synthesized ZnO and the doped derivatives (20–44 m^2 g^{-1}) were consistent with the value of 50 m^2 g^{-1} for commercial FZO-50 (Table 1).

The XRD patterns measured for the pristine and modified ZnO samples are depicted in Fig. 1. All samples exhibited peaks derived from a wurtzite crystal structure [23–25], and the peaks were as-

Table 1
Physicochemical characterization of spheroidal ZnO, rod-like ZnO, Cu–spheroidal ZnO (0.5 wt.% Cu), Ce–spheroidal ZnO, S–ZnO, and commercial ZnO (FZO–50).

Entry		S_{BET} ($m^2 g^{-1}$)	E_g (eV)					Unit cell of wurtzite		Average particle size		
			Extrapolated	Fit to $\alpha \times h\nu \propto (h\nu - E_g)^n$				a (nm)[a]	c (nm)[b]	t (nm)[c]	t_{major} (nm)[d]	t_{minor} (nm)[d]
				$n = 1/2$	3/2	2	3					
a	Spheroidal ZnO	35	3.21	3.24	3.18	3.16	3.07	0.3254	0.5211	39	46.9	22.2
b	Rod-like ZnO	20	3.21	3.25	3.17	3.13	3.06	0.3249	0.5204	48		
c	Cu–spheroidal ZnO	39	3.19	3.22	3.16	3.14	3.09	0.3255	0.5211	34	35.1	23.5
c′	Cu–spheroidal ZnO-reduced	–	3.17	3.21	3.13	3.09	3.03	–	–	–	–	–
d	Ce–spheroidal ZnO	44	3.19	3.24	3.16	3.13	3.07	0.3251	0.5205	34	33.0	18.4
e	S–ZnO	26	3.22	3.27	3.18	3.15	3.09	0.3254	0.5211	38		
f	FZO-50	50	3.24	3.27	3.21	3.18	3.14	–	–	21		

[a] Based on $(10\bar{1}0)$ X-ray diffraction peak position.
[b] Based on (0002) X-ray diffraction peak position.
[c] Based on Scherrer equation: $t = \frac{0.9\lambda}{Peak\_width \cos \theta_B}$.
[d] Based on SEM photographs.
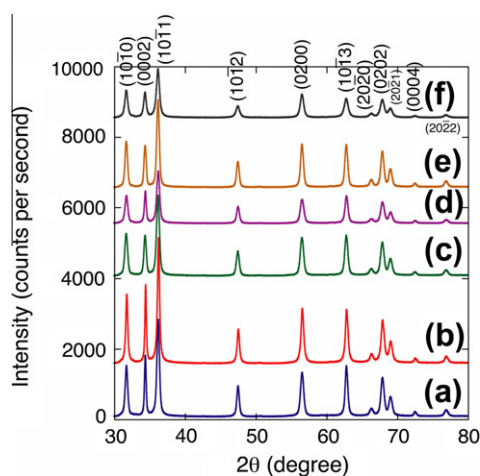
Fig. 1. XRD patterns of fresh samples of spheroidal ZnO (a), rod-like ZnO (b), Cu–spheroidal ZnO (0.5 wt.% Cu; c), Ce–spheroidal ZnO (0.5 wt.% Ce; d), S–ZnO (e), and commercial ZnO (FZO-50, Ishihara Sangyo; (f)).

signed as in Fig. 1. Peaks due to impurities were not detected in all samples. Based on the diffraction angles for the $(10\bar{1}0)$ and (0002) peaks, the lengths a and c of the unit cell were found to be nearly constant at 0.3249–0.3255 nm and 0.5204–0.5211 nm (Table 1), respectively, which are similar to the values for the wurtzite ZnO crystal ($a = 0.325$ nm, $c = 0.5207$ nm) [23].

Whereas for S–ZnO and FZO-50, the intensity ratio of the three peaks in the range of $2\theta_B = 30$–$40°$ was $(10\bar{1}0):(0002):(10\bar{1}1) =$ 52–57:48–53:100 (Fig. 1e and f), the intensity ratio of the spheroidal and rod-like ZnO and Ce–spheroidal ZnO peaks was 53–55:62–64:100 (Fig. 1a, b, and d). The significantly greater intensity of the (0002) peak for the spheroidal and rod-like ZnO and Ce–spheroidal ZnO suggested preferable crystalline growth along the c-axis direction. For Cu–spheroidal ZnO, the intensity ratio of the three peaks was $(10\bar{1}0):(0002):(10\bar{1}1) = 52:50:100$, which was nearly equivalent to that for S–ZnO (52:48:100). The typical trend of the greater (0002) peak intensity for spheroidal ZnO was suspended when the Cu ions were adsorbed probably because of partial dissolution and recrystallization during ion exchange (Fig. 1c).

A representative SEM image for spheroidal ZnO is depicted in Fig. 2A1 and B1. The size distribution along the minor axis was narrow and centered at 22.2 nm (Fig. 2C1), whereas that along the major axis was larger and centered at 46.9 nm (Table 1a), suggesting that the growth of ZnO proceeds along the direction of the c-axis in ethanol. The preferential growth along the c-direction was in agreement with the interpretation based on XRD (Fig. 1a).

The size distribution along the minor axis in the representative SEM image for Cu–spheroidal ZnO (Fig. 2A2 and B2) was centered at 23.5 nm, indicating a negligible change compared with that for spheroidal ZnO. In contrast, the size distribution along the major axis became larger compared with that for spheroidal ZnO and the center decreased to 35.1 nm (Fig. 2C2 and Table 1c). This trend of size distribution along the major axis was also evident for Ce–spheroidal ZnO, which was centered at 33.0 nm (Fig. 2A3, B3, and C3). In addition, the size distribution along the minor axis was clearly smaller and centered at 18.4 nm compared with 22.2–23.5 nm for spheroidal ZnO and Cu–spheroidal ZnO.

A representative SEM image for rod-like ZnO is depicted in Fig. 2A4 and B4. The distribution of the length and diameter is shown in Fig. 2C4. The average size of 79.8 nm × 443 nm combined with the observation of the relatively larger (0002) XRD peak (Fig. 1b) suggested preferable crystalline growth along the c-direction.

In the high-resolution TEM images for spheroidal ZnO, hexagonal shapes were clearly observed (Fig. 3a1 and a3) viewed from [0001] direction, in addition to spheroids (a1, a3, a5) that were already observed in SEM (Fig. 2B1). In the image a4 of Fig. 3, the $(10\bar{1}0)$ lattice pattern with a spacing of 0.273 nm was observed in agreement with $\frac{\sqrt{3}}{2}a$ (=0.281 nm) for the wurtzite crystal structure. Rotated by 30° from the $(10\bar{1}0)$ lattice pattern, the $(11\bar{2}0)$ lattice pattern with a spacing of 0.158 nm was also observed in agreement with $\frac{a}{2}$ (=0.163 nm). The crystal growth direction in ethanol was [0001] direction as observed in images a6 and a7 in which the (0002) lattice pattern with a spacing of 0.251 nm was observed in agreement with $\frac{c}{2}$ (=0.2604 nm). In the high-resolution TEM images b5 and b7 of Fig. 3 for rod-like ZnO, the lattice pattern with a spacing of 0.275–0.276 nm was parallel to the major axis of ZnO rods. This is the $(10\bar{1}0)$ lattice pattern viewed from the $(1\bar{2}10)$ direction in agreement with $\frac{\sqrt{3}}{2}a$ (=0.281 nm).

The UV–visible spectra for the pristine and modified ZnO samples are summarized in Fig. 4. The absorption edge was extrapolated, and the intersection with the x-axis (Fig. 4, inset) was estimated for each bandgap value (Table 1). The bandgap reduced in the order of FZO-50 (f, 3.24 eV) > S–TiO$_2$ (e, 3.22 eV) > rod-like ZnO (b, 3.21 eV) $\sim$ spheroidal ZnO (a, 3.21 eV) > Ce–spheroidal ZnO (d, 3.19 eV) $\sim$ Cu–spheroidal ZnO (c, 3.19 eV) > Cu–spheroidal ZnO-reduced (c′, 3.17 eV). The foot of the absorption edge was clearly extended to the visible light region for Cu–spheroidal ZnO-reduced (Fig. 4c′).

For the three ZnO samples, the Davis–Mott equation was fit to the UV–visible absorption data with n values between 1/2 and 3 (Table 1a, b, and f). The fitting provided E_g values of 3.17–3.27 eV with n values between 1/2 and 3/2, similar to those estimated from the simple extrapolation of the absorption edge (3.21–3.24 eV).
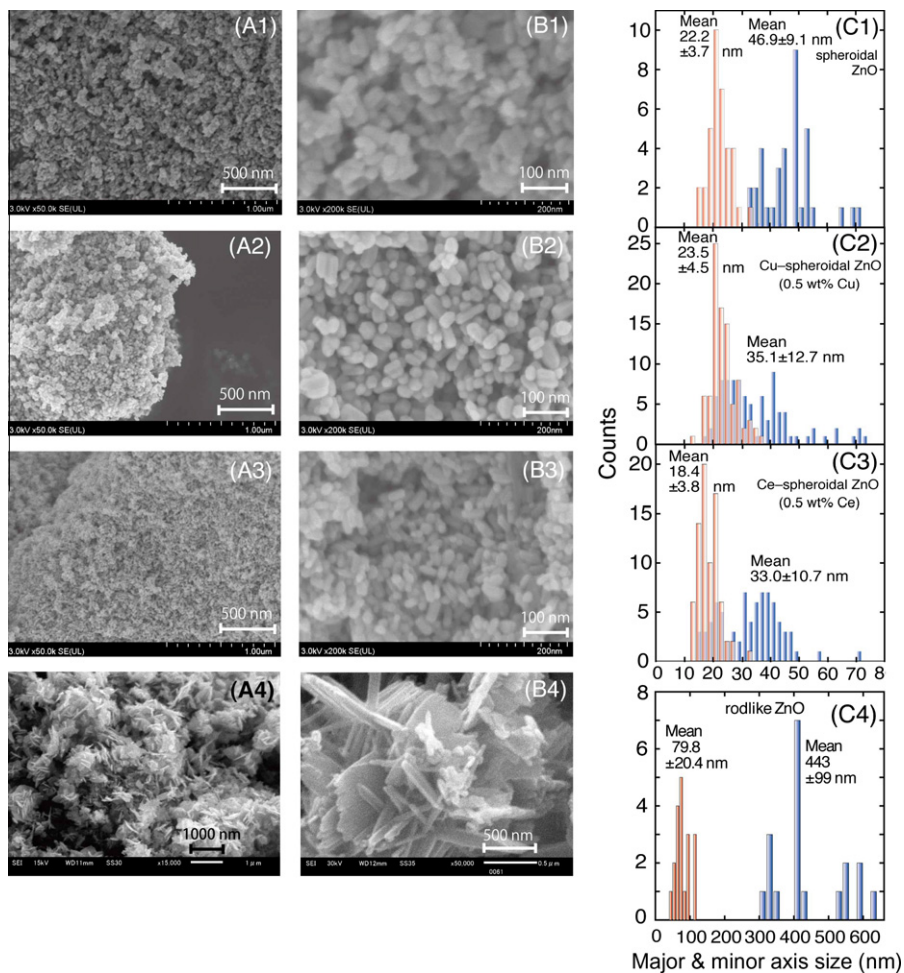
Fig. 2. SEM images for spheroidal ZnO (A1 and B1), Cu–spheroidal ZnO (A2 and B2), Ce–spheroidal ZnO (A3 and B3), and rod-like ZnO (A4 and B4), and the size distribution along the major and minor axes for the projected ellipses (C1–3) and the length and diameter of nanorods (C4).
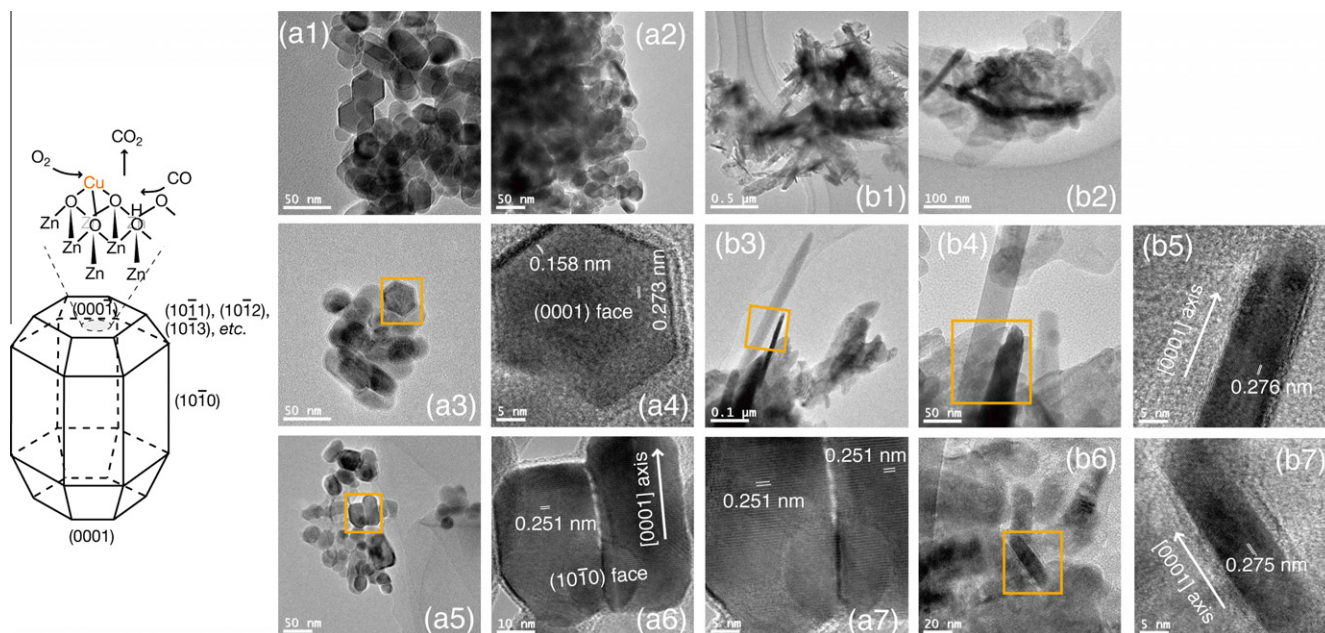
Fig. 3. High-resolution TEM images for spheroidal ZnO (a1–a7) and rod-like ZnO (b1–b7) and a model of ZnO spheroidal crystal.
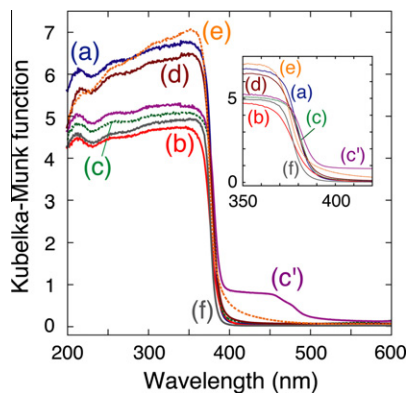
Fig. 4. Diffuse reflectance UV–visible absorption spectra of fresh samples of spheroidal ZnO (a), rod-like ZnO (b), Cu–spheroidal ZnO (0.5 wt.% Cu; (c)), c was reduced with ethanol under UV–visible light (c′), Ce–spheroidal ZnO (0.5 wt.% Ce; (d)), S–ZnO (e), and commercial ZnO (FZO-50; (f)). (Inset) Enlarged view of the absorption edge between 350 and 420 nm.

The nature of electronic transition did not change when Cu^{2+} or Ce^{3+} was adsorbed on spheroidal ZnO or when S was doped in ZnO. The E_g values estimated on the basis of the simple extrapolation were 3.19–3.22 eV, similar to values given by fitting to the Davis–Mott equation with n values between 1/2 and 3/2 (Table 1c–e).

The FT-IR spectra were measured for Cu–spheroidal ZnO. After the as-prepared sample was held in a vacuum for 2 h, a shoulder peak and an accompanying broad peak appeared centered at $3666\ cm^{-1}$ and $3310\ cm^{-1}$, respectively. When CO (46 Pa) was introduced, two new peaks were observed at $1630\ cm^{-1}$ and $1339\ cm^{-1}$. At 46 Pa of CO and 46 Pa of O_2 under UV–visible light, peaks at 2985, 2879, 1627, 1587, and $1297\ cm^{-1}$ were observed. On the other hand, peaks appeared at 2952, 2877, 2746, 1645, 1620, and $1320\ cm^{-1}$ when formic acid (46 Pa) was introduced to Cu–spheroidal ZnO.

3.2. Cu K-edge XANES

The Cu K-edge X-ray absorption near-edge structure (XANES) spectrum for the fresh Cu–spheroidal ZnO catalyst is shown in Fig. 5A–a. The Cu valence state was II in fresh Cu–spheroidal ZnO. A tiny 1s–3d pre-edge peak was observed at 8979 eV [26]. After illumination for 1 min under UV–visible light, a weak shoulder peak began to appear at 8983.1 eV (Fig. 5A–b). The shoulder peak intensity grew gradually to 0.0727 under UV–visible illumination for 3 h (Fig. 5A–d). One minute after the UV–visible light

was removed, the peak intensity at 8983.1 eV reduced by 0.0035 (Fig. 5A–e).

The background and peak intensities at 8983.1 eV for as-synthesized Cu–spheroidal ZnO (Cu^{II} sites only) and Cu–spheroidal ZnO-reduced (Cu^{I} sites only) are indicated by dotted lines in Fig. 5B. The Cu–spheroidal ZnO-reduced sample was prepared by UV–visible illumination for 1 h and the UV–visible (Fig. 4c′) and X-ray (Fig. 5A–f) absorption spectra changed negligibly following UV–visible illumination for 1–3 h. The weak 1s–3d pre-edge peak at 8979 eV for as-synthesized Cu–spheroidal ZnO diminished for Cu–spheroidal ZnO-reduced. The shoulder peak at 8983.1 eV can be understood to originate from Cu^{I} sites because a similar shoulder peak was reported for Cu_2O at a distinctly lower energy than the absorption edge for CuO [27,28]. The Cu K-absorption edge energy negligibly changed at 8992.9–8993.1 eV when the Cu^{II} sites were reduced to Cu^{I} sites [29]. Therefore, the Cu^{I}-site ratio in the sample was approximated using the following equation:

$$Cu^{I}\text{-site ratio} \sim \frac{\text{Peak intensity@8983.1 eV} - 0.048\ (\text{for }Cu^{II}\ 100\%)}{0.21(\text{for }Cu^{I}\ 100\%) - 0.048\ (\text{for }Cu^{II}\ 100\%)}.$$

Based on this approximation, 3.9% of Cu^{I} sites were formed in the initial 1 min, and this population gradually increased to 15.6% after 3 h of UV–visible illumination. When the UV–visible illumination was removed, the Cu^{I} population dropped to 13.4%. Cu^{II} and Cu^{I} sites were found to be in a dynamic equilibrium in a steady-state population of transmitted electrons that were photogenerated and did not recombine with holes during the diffusion to surface, as given by the following equation:

$$K = \frac{[Cu^{I}]}{[Cu^{II}]\left[e^{-}_{\text{diffused to surface}}\right]}.$$

3.3. Photo-PROX reactions of CO

First, CO photo-PROX reaction tests were performed using synthesized and commercial ZnO samples, beginning with the initial pressures of CO (63 Pa), O_2 (76 Pa), and H_2 (6.3 kPa) under UV–visible light for 5 h. The initial formation rates of CO_2 within 1 h were in the following order: spheroidal ZnO (17 µmol h^{-1} g^{-1}_{cat}) > FZO-50 (13 µmol h^{-1} g^{-1}_{cat}) ≫ rod-like ZnO (0.42 µmol h^{-1} g^{-1}_{cat}) (Table 2A, B, and P, Fig. 6A, B, and I). The rates were not correlated to each specific surface area (35, 50, and 20 m² g^{-1}, respectively; Table 1), suggesting that the catalytic reactivity critically depended on the exposed crystal face. Selectivity to CO_2 was 92–89 mol% for spheroidal ZnO and FZO-50, whereas it was quite poor (53 mol%) for rod-like ZnO (Table 2A, B, and P).
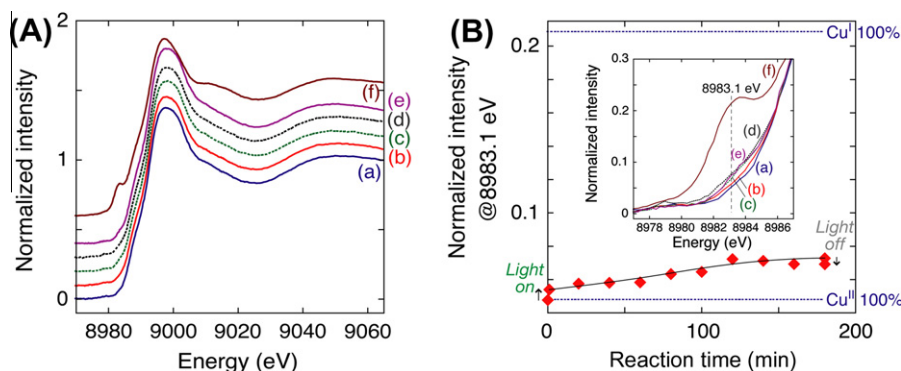
Fig. 5. (A) Normalized Cu K-edge XANES spectra for Cu–spheroidal ZnO before illumination (a), at 1 (b), 80 (c), and 180 min (d) from the start of illumination of UV–visible light (500-W Xe arc lamp) with the initial pressures of CO (135 Pa), O_2 (270 Pa), and H_2 (13 100 Pa), and at 1 min after the illumination (e) for Cu–spheroidal ZnO-reduced (f). (B) The intensity change of a shoulder peak at 8983.1 eV during the illumination of UV–visible light and the intensity for as-prepared Cu–spheroidal ZnO (Cu^{II} 100%) and Cu–spheroidal ZnO-reduced (Cu^{I} 100%). (Inset) Enlarged pre-edge region of spectra in panel A.

Table 2
Preferential oxidation rates of CO in H_2 and O_2 using the synthesized ZnO samples: Cu–spheroidal ZnO (0.5 wt.% Cu), Ce–spheroidal ZnO, S–ZnO, commercial ZnO (FZO–50), and reference catalysts.[a]

Entry	Catalyst	Light	Initial gas (Pa)			Time (h)	1st order rate constant k (min^{-1})	Initial formation rates of CO_2 (μmolh^{-1}g$_{cat}^{-1}$)[b]	Conversion to CO_2 (%)[c]	Selectivity to CO_2 (mol%)[d,e]	Reference
			CO	H_2	O_2						
A	Spheroidal ZnO	UV–visible	63	6300	76	5	0.0162	17	52	92[d]	This work
B	Rod-like ZnO	UV–visible	63	6300	76	5	0.0001	0.42	3.4	53[d]	This work
C	Cu (0.5 wt%)–spheroidal ZnO	UV–visible	63	6300	76	3	0.0249	56	91	99[d]	This work
C′	Cu (0.5 wt%)–spheroidal ZnO-reduced	UV–visible	63	6300	76	3	0.0242	51	86	98	This work
C″	Cu (0.01 wt%)–spheroidal ZnO	UV–visible	63	6300	76	3	0.0204	27	69	97[d]	This work
C‴	Cu (0. 1 wt%)–spheroidal ZnO	UV–visible	63	6300	76	3	0.0305	77	100	96[d]	This work
C⁗	Cu (1.0 wt%)–spheroidal ZnO	UV–visible	63	6300	76	3	0.0181	40	91	96[d]	This work
D	Cu (0.5 wt%)–spheroidal ZnO	UV–visible	63	6300	150	3	0.0341	84	100	94[d]	This work
E		UV–visible	63	0	150	1.5	0.0829	94	100	97[d]	This work
F		UV–visible	63	600	150	2	0.0430	61	62	99[d]	This work
G		UV–visible	63	3000	150	3	0.0342	70	69	98[d]	This work
H		UV–visible	63	63,000	150	3	0.00709	18	66	79[d]	This work
I		UV–visible	0	0	0	3	–	6.2	–	–	This work
J		Visible[f]	63	6300	150	3	0.0005	1.5	6.5	86[d]	This work
K		No light (290 K)	63	6300	150	3	0.0004	0.42	0.86	100[d]	This work
K′		No light (327 K)	63	6300	150	3	0.0007	2.2	5.1	79[d]	This work
L	Cu (0.5 wt%)–spheroidal ZnO[g]	UV–visible	63	6300	150	3	0.00775	1.5	43	99.6[d]	This work
M	Ce (0.5 wt%)–spheroidal ZnO	UV–visible	63	6300	150	3	0.0172	44	51	99[d]	This work
N	S–ZnO	UV–visible	63	6300	76	3	0.0009	2.4	4.2	92[d]	This work
O		Visible[f]	63	6300	76	3	0.0007	0.88	2.2	90[d]	This work
P	FZO-50	UV–visible	63	6300	76	5	0.0157	13	42	89[d]	This work
Q	NiO/TiO$_2$	UV–visible	92	590	180	3	–	38	81	98[e]	[9]
R	Mo/SiO$_2$	UV–visible	92	590	180	3	–	95	~100	99[e]	[10]
S	Au–TiO$_2$	No light (290 K)	63	6300	150	1	0.141	1200	100	93[d]	This work
T	Reactor only	UV–visible	63	6300	150	3	0.0001	–	2.9	77[d]	This work
U		Visible[f]	63	6300	150	3	0.0004	–	11	90[d]	This work

[a] Catalyst 50 mg except for Au/TiO$_2$ (11 mg).
[b] In initial 0.25, 0.5, or 1 h.
[c] (Molar amount of CO_2 formed at the end of reaction test)/{initial molar amount of CO (3.7 μmol)} × 100.
[d] (Molar amount of CO_2 formed)/(molar amounts of CO_2 + H_2O formed) × 100.
[e] (Molar amount of CO_2 formed)/(initial molar amount of H_2 − final molar amount of H_2 + molar amounts of CO_2 formed) × 100.
[f] >420 nm using L-42 filter.
[g] Preheated in air at 573 K for 2 h.
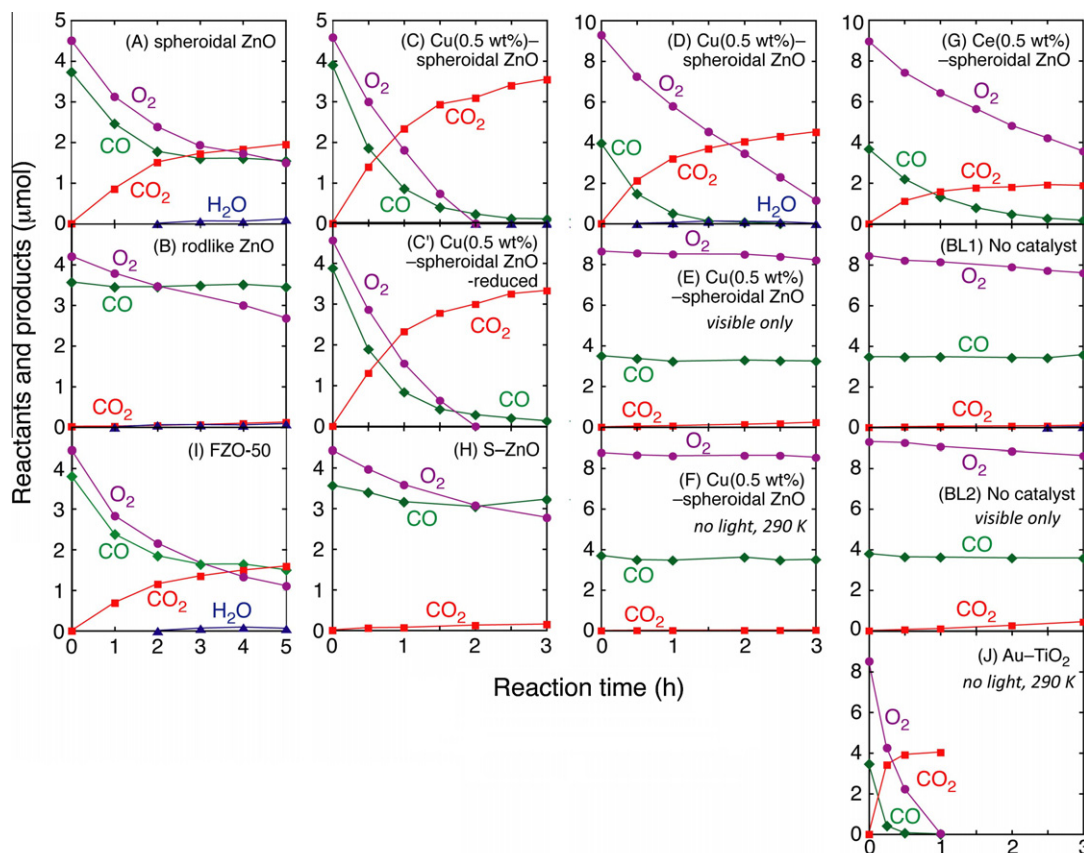
Fig. 6. Time course of the PROX reaction of CO in H_2 using spheroidal ZnO (A), rod-like ZnO (B), Cu–spheroidal ZnO (C–F), Cu–spheroidal ZnO-reduced (C'), Ce–spheroidal ZnO (G), S–ZnO (H), FZO-50 (I), and Au–TiO$_2$ (J) illuminated with UV–visible light except for E, BL2 (visible light), and F, J (no light). No catalyst charged for control tests (BL1, BL2). Reaction gases: CO 3.7 μmol (63 Pa), H_2 370 μmol (6.3 kPa), and O_2 4.5 μmol (76 Pa) (A–C, C', H, I) or O_2 9.0 μmol (150 Pa) (D–G, J, BL1, BL2).

Next, the most active spheroidal ZnO among the tested ZnO samples was adsorbed with Cu ions or doped with S. The photo-PROX tests of CO using adsorbed/doped catalysts were conducted under the same conditions as for undoped ZnO samples, but for 3 h. The initial CO_2 formation rate for Cu–spheroidal ZnO increased by a factor of 3.3, while the rate for S–TiO$_2$ decreased by a factor of 0.14, both compared with that for spheroidal ZnO (Fig. 6A, C, and H, Table 2C and N). Selectivity to CO_2 was improved from 92 mol% to 99 mol% by the addition of Cu^{2+} to spheroidal ZnO. The initial 9800 ppm concentration of CO was decreased to 280 ppm following the 3-h photoreaction (Fig. 6C). All the supplied O_2 was consumed within 2 h, and further removal of CO did not proceed. Furthermore, Cu–spheroidal ZnO-reduced was tested under photocatalytic reaction conditions (Fig. 6C'). The result was essentially identical to that observed for Cu–spheroidal ZnO (Table 2C and C').

The dependence of CO photo-PROX reactivity on the content of Cu was also tested for Cu–spheroidal ZnO between 0.01 and 1.0 wt.% of Cu (Table 2C″, C‴, C, C⁗). Initial formation rates of CO_2 and the conversion to CO_2 were greatest in the case of 0.1 wt.% Cu (77 μmol h^{-1} g$_{cat}^{-1}$ and 100%, respectively), whereas the selectivity to CO_2 was best in the case of 0.5 wt.% Cu (99 mol%).

Next, the partial pressure of O_2 was increased from 76 Pa to 150 Pa (63 Pa of CO and 6.3 kPa of H_2). The initial formation rate of CO_2 increased by a factor of 1.5, and selectivity to CO_2 was 94 mol% (Table 2D). In this test, the initial 9 700 ppm concentration of CO was decreased to 21 ppm in 3 h and 0.35 ppm in 5 h (Fig. 6D). The adsorbed Ce ions also promoted the photo-PROX reaction of spheroidal ZnO (Fig. 6G and Table 2M). However, the initial CO_2 formation rate was 52% compared with that for Cu–spheroidal ZnO (Table 2D). As-prepared Cu–spheroidal ZnO powder was calcined at 573 K for 2 h, and the photo-PROX test was performed

(Table 2L). While selectivity to CO_2 remained at 99.6 mol%, the initial CO_2 formation rate decreased to 1.9% of that for as-prepared Cu–spheroidal ZnO.

The photo-PROX tests under visible light alone (>420 nm) were conducted for Cu–spheroidal ZnO and S–ZnO. With the initial pressures of CO (63 Pa), O_2 (150 Pa), and H_2 (6.3 kPa), the initial CO_2 formation rate for Cu–spheroidal ZnO decreased to as low as 1.8% compared with that for Cu–spheroidal ZnO excited under UV–visible light (Table 2D and J, Fig. 6D and E). S–ZnO was found to be inactive (Table 2O).

For Cu–spheroidal ZnO, by setting the initial pressures of CO at 63 Pa and O_2 at 150 Pa, the dependence of the reaction on the H_2 pressure was examined between 0 kPa and 63 kPa (Table 2D–H). As the partial pressure of H_2 increased, the initial CO_2 formation rates decreased from 94 μmol h^{-1} g$_{cat}^{-1}$ to 18 μmol h^{-1} g$_{cat}^{-1}$. Selectivity to CO_2 was excellent (99–97 mol%) when the H_2 pressure was 0–3.0 kPa, but decreased to 94 mol% at an H_2 pressure of 6.3 kPa and then to 79 mol% at an H_2 pressure of 63 kPa.

The amount of Cu–spheroidal ZnO photocatalyst was varied between 25 and 100 mg for photo-PROX reaction tests of CO (Fig. 7A). The (pseudo) first-order reaction rate constants k based on the decreasing rates of CO (Section 2.4) linearly increased as a function of catalyst amount charged. Further, transmitted UV–visible light linearly decreased when the homogeneously spread catalyst amount increased up to 0.5 g (Fig. 7B). Thus, absorbed photon numbers by photocatalysts (typically 50 mg) were proportional to the amount of photocatalysts in this study, and the catalytic rates (Table 2) were expressed per catalyst amount (g$_{cat}$).

In the absence of a catalyst, the photoreaction proceeded under UV–visible light, but CO conversion to CO_2 was only 2.9% after 3 h (Fig. 6BL1 and Table 2T). Surprisingly, the photoreaction performed
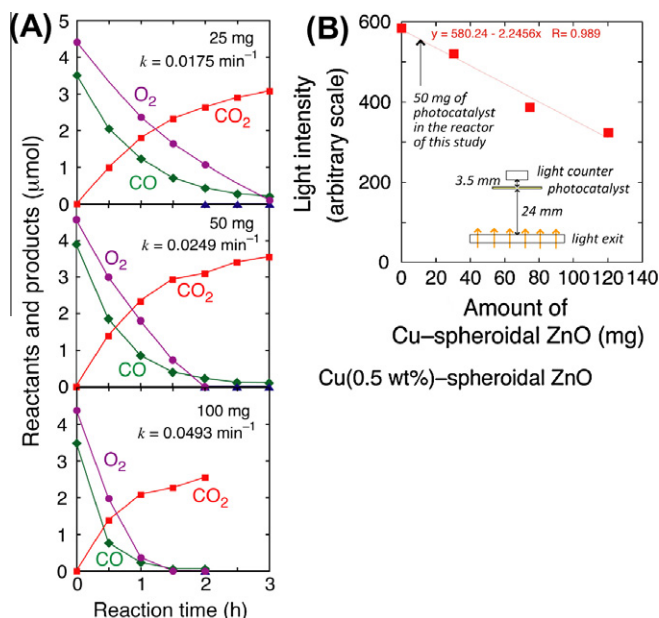
Fig. 7. (A) Dependence of time course of the PROX reaction of CO in H_2 on the amount of Cu–spheroidal ZnO used (25–100 mg) illuminated with UV–visible light. Reaction gases: CO 3.7 μmol (63 Pa), H_2 370 μmol (6.3 kPa), and O_2 4.5 μmol (76 Pa). (B) Dependence of transmitted UV–visible light intensity through the 30–120 mg of Cu–spheroidal ZnO in the area of 5.3 cm^2. The distance between the bottom of the reactor and the lamp exit was set to 24 mm.

under visible light alone converted a greater amount of CO to CO_2 after 3 h (11%) (Fig. 6BL2 and Table 2U). The photoreaction under UV light appears to be unselective, and some amount of the O_2 gas was consumed through reaction with H_2. On the other hand, the photoreaction under visible light was more selective (90 mol% compared to 77 mol% selectivity under UV–visible light) and formed a larger amount of CO_2.

In the absence of light at 290–327 K, Cu–spheroidal ZnO converted 0.86–5.1% of CO to CO_2 after 3 h (Table 2K, K′ and Fig. 6F). In the photocatalytic tests in Table 2D, the temperature was 305 K at the catalyst position. Further, the obtained first-order rate constant at 290–327 K (0.0004–0.0007 min^{-1}) under dark was only 1.2–2.1% of that under visible light. Thus, thermal PROX reactions of CO were negligible using Cu–spheroidal ZnO. The small but non-zero initial CO_2 formation rate (6.2 μmol h^{-1} g$_{cat}^{-1}$) for Cu–spheroidal ZnO under UV–visible light in the absence of reaction gases (Table 2I) may be because of the impurity carbonates pre-adsorbed on the ZnO surface.

For comparison with the photo-PROX reactions, the PROX reaction of CO in the absence of light at 290 K using an Au–TiO_2 catalyst was examined starting with initial pressures of CO (63 Pa), O_2 (150 Pa), and H_2 (6.3 kPa) (Fig. 6J and Table 2S). The initial CO_2 formation rate was 14 times greater compared with that for Cu–spheroidal ZnO under UV–visible light (Table 2D). Furthermore, selectivity to CO_2 was comparable (93–94 mol%). In addition, the photo-PROX test of CO was performed using Au–TiO_2 under UV–visible light; however, except for an increase in water formation by a factor of 1.2, the effect of light was negligible.

4. Discussion

4.1. Syntheses and properties of ZnO-based photocatalysts

Spheroidal and rod-like ZnO particles were synthesized. The spheroidal and rod-like particle shape in the SEM images (Fig. 2B1 and B4) and the greater intensity of the (0002) peak in the XRD patterns compared with the (10$\bar{1}$0) and (10$\bar{1}$1) peaks

(Fig. 1a and b) indicate that the particles grew anisotropically along the c-axis direction [30] to preferentially expose the polar (0001) face [27]. High-resolution TEM images demonstrated the (10$\bar{1}$0), (11$\bar{2}$0), and (0002) lattice pattern and crystal growth direction of [0001] for spheroidal ZnO (Fig. 3a1–7). For the spheroids, a model of spheroid consisted of (0001), (10$\bar{1}$0), (000$\bar{1}$), and (10$\bar{1}$n) was proposed (Fig. 3, model on left). The S_{BET} value for spheroidal ZnO (35 m^2 g^{-1}) was an intermediate between the values for FZO-50 (50 m^2 g^{-1}) and rod-like ZnO (20 m^2 g^{-1}; Table 1), and those for Cu–spheroidal ZnO and Ce–spheroidal ZnO (39–44 m^2 g^{-1}) were greater compared with spheroidal ZnO. A reason for this was the partial dissolution and recrystallization of spheroidal ZnO during the Cu/Ce ion exchange in the metal nitrate solution. Based on the relative intensity of the (0002) XRD peaks, for Ce–spheroidal ZnO, the anisotropic particle shape was preserved (Fig. 1d, Fig. 2A3 and B3), whereas for Cu–spheroidal ZnO, the particle shape became similar to that of general ZnO crystals (Figs. 1c and 2 A2 and B2).

The E_g values were estimated on the basis of the UV–visible absorption spectra for the ZnO samples and the heteroatom adsorbed/doped ZnO samples (Fig. 4). The E_g values were evaluated by the extrapolation of the absorption edge to the x-axis. The value for FZO-50 (3.24 eV) was 0.03 eV greater than those for spheroidal and rod-like ZnO (3.21 eV; Table 1a, b, and f) probably because of the nanosize effect [24] of the smaller particles of FZO-50 (21 nm, average) compared with those of spheroidal and rod-like ZnO (average 39–48 nm based on XRD, Table 1).

The adsorption of Cu^{2+} or Ce^{3+} on spheroidal ZnO decreased the E_g values by 0.02 eV [25]. The E_g value further decreased by 0.02 eV when Cu^{2+} was reduced to Cu^+ under UV–visible light in the presence of ethanol (Table 1c′). It is known that the electronic transition of ZnO is direct [31]. For all ZnO-based samples synthesized in this study, the E_g values estimated by the simple absorption edge extrapolation were in agreement with those given by fitting to the Davis–Mott equation with n values between 1/2 and 3/2 (Table 1). Thus, the electronic transition was direct from 2p of O to the following: 4s or 4p of Zn; 3d, 4s, or 4p of Cu; and 6s or 4f of Ce.

4.2. Optimization of photo-PROX of CO

Among the ZnO samples tested for photo-PROX reactions, spheroidal ZnO exhibited the highest CO_2 formation rates (Table 2A, B, and P). The initial CO_2 formation rate was enhanced by a factor of 3.3, and selectivity to CO_2 was improved to 99 mol% upon the adsorption of Cu^{2+} on spheroidal ZnO (Table 2C). The CO_2 formation rate positively depended on the partial pressure of O_2. Under 63 Pa of CO, 150 Pa of O_2, and 6.3 kPa of H_2, the initial 9 700 ppm concentration of CO was photocatalytically decreased to 21 ppm within 3 h and to 0.35 ppm within 5 h (Table 2D and Fig. 6D), suggesting potential application to purify H_2 to the polymer electrolyte FCs.

In contrast to the promoting effects of adsorbed Cu^{2+} or Ce^{3+} (Table 2C and M), S–ZnO was fairly inactive (Table 2N). The valence of S in the S–ZnO should be negative because ethanethiol was used in the solvothermal synthesis at 433 K and obtained powder was not calcined. The anionic S atoms may block the surface active sites of Zn for the photo-PROX reaction of CO [15].

The initial CO_2 formation rate of Cu–spheroidal ZnO photocatalyst decreased to only 1.9% of the incipient one when it was calcined at 573 K (Table 2L). We suspect that adsorbed Cu^{2+} sites for incipient Cu–spheroidal ZnO became doped in/on ZnO and/or aggregated at 573 K and became less reactive based on the change of coordination number of Cu–O from 6 to 4 by Cu K-edge EXAFS analyses. It is also plausible that the surface hydroxy groups decreased by the heating at 573 K and the catalytic step(s) involving hydroxy group became quite slower.

UV light illumination was essential for the photo-PROX activity of Cu–spheroidal ZnO because the initial CO_2 formation rate was only 1.8% under visible light alone (>420 nm; Table 2J and D). This dramatic decrease in reactivity was in accordance with the UV–visible spectrum (Fig. 4c); the absorption tail negligibly extended to more than 420 nm.

In addition, the photo-PROX activity of the Cu–spheroidal ZnO photocatalyst depended on the partial pressure of H_2 between 0 kPa and 63 kPa (Table 2D–H). As the partial pressure of H_2 increased, the initial CO_2 formation rate and CO_2 selectivity gradually decreased from 94 $\mu mol\ h^{-1}\ g_{cat}^{-1}$ to 18 $\mu mol\ h^{-1}\ g_{cat}^{-1}$ and from 99–97 mol% to 79 mol%, respectively. The effect of the presence/absence of H_2 has previously been reported for the PROX reaction of the Au–TiO_2 catalyst [32]. The reaction order of P_{CO} clearly increased from 0.34 to 0.82 owing to the presence of H_2, that is, poor PROX activity for low concentration of CO in predominant H_2.

Considering the dependence on the partial pressure of H_2, the photo-PROX results for Cu–spheroidal ZnO at an H_2 pressure of 600 Pa were compared with literature data for NiO/TiO_2 and Mo/SiO_2 tested with an H_2 pressure of 590 Pa [9,10] (Table 2F, Q, and R). The initial CO_2 formation rates were in the order of Mo/SiO_2 > Cu–spheroidal ZnO > NiO/TiO_2. Furthermore, selectivity to CO_2 was in the order of Cu–spheroidal ZnO $\sim$ Mo/SiO_2 > NiO/TiO_2.

In the absence of photocatalysts, 2.9–11% of CO was converted to CO_2 in 3 h, whereas in the presence of Cu–spheroidal ZnO, 100% of CO was converted to CO_2 (Table 2D, T, and U). The contribution of the photoreaction was small under UV–visible light. Under visible light, the conversion to CO_2 was 11% in the absence of catalyst (Table 2U, Fig. 6BL2), while the conversion was only 6.5% in the presence of Cu–spheroidal ZnO (Table 2J, Fig. 6E). Unfortunately, Cu–spheroidal ZnO was poorer than photochemical reaction under visible light and a part of low concentration of CO_2 formed would be adsorbed on Cu–spheroidal ZnO, as shown in Fig. 6E. The relatively greater amount of O_2 decreased, as shown in Fig. 6BL1 and BL2, compared to formed amount of CO_2. This was due to water formation especially for BL1, but the low concentrations of water adsorbed in the reaction glass tube and were not detected in the time course. Quantitative (but still small amount of) water was detected when the reaction gas was collected in liquid nitrogen trap after the reaction tests (Table 2T and U). In the absence of light, Cu–spheroidal ZnO converted only 0.86–5.1% of CO to CO_2 at 290–327 K in 3 h (Table 2K and K'). Spheroidal ZnO and Cu–spheroidal ZnO were excellent catalysts for the photo-PROX of CO but poor catalysts for the PROX of CO at 290–327 K.

4.3. Reaction mechanism of photo-PROX of CO using Cu–spheroidal ZnO

During the photo-PROX reaction, the initial rates of decrease in CO and O_2 gases were essentially equivalent for spheroidal ZnO, Ce–spheroidal ZnO, and FZO-50 on a molar amount basis (Fig. 6A, G, and I). In contrast, CO initially decreased more rapidly than O_2 for Cu–spheroidal ZnO (Fig. 6C and D), which corresponds better to the stoichiometric ratio of the reaction $2CO + O_2 = 2CO_2$. In contrast, the molar amount of O_2 decreased more rapidly than that of CO for rod-like ZnO, S–ZnO, and Au–TiO_2 (Fig. 6B, H, and J).

The ratio of CO_2 formed versus CO diminished suggested differences in the catalytic mechanism. The ratio was close to unity for spheroidal ZnO (89%), rod-like ZnO (99%), Cu–spheroidal ZnO (93–100%), and Au–TiO_2 (100%), whereas it was lower for FZO-50 (69%), Ce–spheroidal ZnO (54%), and S–ZnO (43%) (Fig. 6I, G, and H). The catalysts that do not remain CO-derived species on the surface exhibited higher CO_2 formation rates.

During the photo-PROX reaction, the change in the valence state of Cu adsorbed on spheroidal ZnO was monitored using Cu K-edge XANES (Fig. 5). The ratio for Cu^I sites was 3.9% in the initial 1 min

and progressively increased to 15.6% over the 3-h photo-PROX reaction, maintaining dynamic equilibrium. The stabilization of Cu^I over basic ZnO was suggested [33]. The growing rate of Cu^I sites under UV–visible illumination was 4.1 $\mu mol - Cu\ h^{-1}\ g_{cat}^{-1}$ in 135 Pa of CO, 270 Pa of O_2, and 13.1 kPa of H_2. The photo-PROX reaction rate to form CO_2 under these reaction conditions was 29.3 $\mu mol - CO_2\ h^{-1}\ g_{cat}^{-1}$ (kinetic data not shown). Therefore, the reduction of Cu^II to Cu^I sites detected by Cu K-edge XANES was not a direct step incorporated in the photo-PROX reaction mechanism of CO, but non-catalytic step to accumulate Cu^I sites.

The CO photo-PROX results were optimum when the Cu content was 0.1–0.5 wt.% (Table 2C'', C''', C, C''''). Small amount of Cu^II sites should be enough to accept photogenerated and diffused electrons in ZnO under the reaction conditions and excessive amount of Cu^II sites than 0.5 wt.% even blocked active sites over ZnO.

When the photo-PROX reaction was performed using Cu–spheroidal ZnO-reduced in which the Cu^II sites were reduced to Cu^I, the results (Table 2C', Fig. 6C') were essentially identical to those obtained using Cu–spheroidal ZnO in which the initial Cu valence was II (Table 2C, Fig. 6C). This can be explained by the fact that Cu^II sites accept diffused photoelectrons in ZnO or prereduced Cu^I sites were set and rapidly transfer them to O_2-derived species; however, these quick steps themselves were not detected by XANES (Fig. 5).

In the photodecomposition of sucrose, Cu^{2+} ions in the aqueous solution increased the photodecomposition rates, and it is proposed that the photogenerated electrons were transferred from TiO_2 to the Cu^{2+} ions in the aqueous solution and then transmitted to oxygen molecules [34]. It is believed that the hole diffusion length is $\sim$10 nm versus the electron diffusion length is $\sim$10 μm in TiO_2 [35]. In ZnO, the hole and electron diffusion lengths are suggested to be 240–440 nm [36,37] and 50–140 μm [38], respectively. Furthermore, direct photoelectronic transition takes place from 2p of O to relatively diffused 4s or 4p of Zn and 3d, 4s, or 4p of Cu in Cu–spheroidal ZnO. Thus, photogenerated electrons could diffuse in entire spheroidal ZnO (35.1 nm × 23.5 nm in average, Fig. 2C2) probably following in the proximity to Zn^{2+} ions to surface Cu^{2+} sites before they recombined with holes. The indirect orbital overlap between diffused 4s or 4p of Zn and 3d, 4s, or 4p of Cu was also suggested at surface [39].

The proposed photo-PROX reaction mechanism is illustrated in Scheme 1. The two routes are not similar to the PROX reaction mechanism where CO adsorption on the metal particle surface and the activation of O_2 at the interface between metal particles and support oxide [32,40] is proposed. The CO molecules react with surface hydroxy to form formates [41] as monitored in FT-IR in Route A. Oxidation of CO coupled with oxygen species at the surface and surface reoxidation using O_2 were proposed for CO oxidation of Co_3O_4 nanorods, predominantly on the (1 1 0) plane [42].

The rod-like ZnO was fairly inactive compared to spheroidal ZnO (Table 2A and B, Fig. 6A and B), and thus, the crystal faces parallel to [0 0 0 1] axis should be inactive. The reactivity difference of crystal faces may be exaggerated because electron–hole pairs photogenerated in rod-like ZnO (443 nm × 79.8 nm in average, Fig. 2C4) mostly diffused to nearer side faces of nanorods and rarely reached to relatively far $(0\,0\,0\,\bar{1})$ face at the end of nanorods. The polar $(0\,0\,0\,\bar{1})$ face terminates O atoms and/or hydroxy group. Because the ion-exchanged Cu^{2+} sites for reduction reaction and formate species starting from CO and hydroxy can be formed in vicinity on $(0\,0\,0\,\bar{1})$ face of Cu–spheroidal ZnO (Fig. 3, model on left), the reduction and oxidation would occur preferably on $(0\,0\,0\,\bar{1})$ face compared to $(1\,0\,\bar{1}\,0)$ and $(1\,1\,\bar{2}\,0)$ face.

In the FT-IR spectrum for ZnO, the absorption peaks of formate species were reported to be due to the antisymmetric ($\nu_{as}(OCO)$) and symmetric stretching vibration of the O–C–O group ($\nu_s(OCO)$) at 1580 cm^{-1} and 1365 cm^{-1}, respectively, the coupling mode of
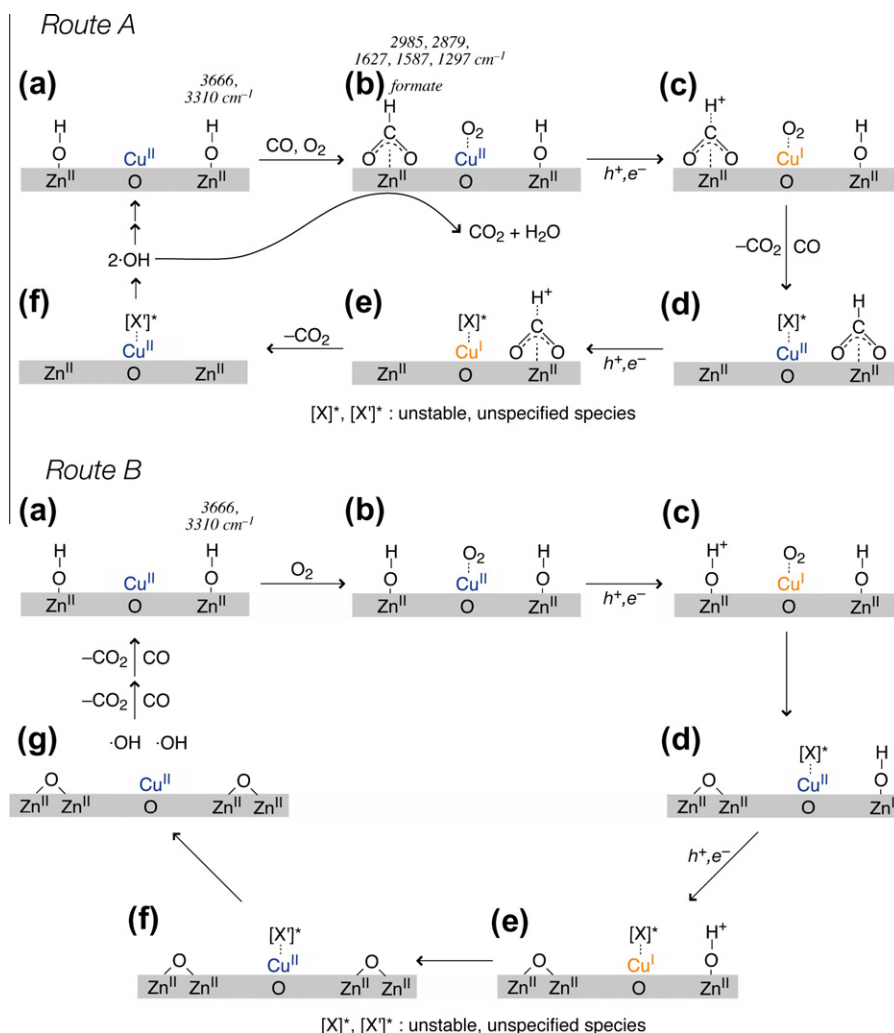
Scheme 1. Proposed mechanism of the photocatalytic PROX reaction of CO using spheroidal ZnO promoted by Cu^{2+} ions. Route A is via the coupling of adsorbed O_2 with formate species, whereas Route B is via the coupling of adsorbed O_2 with surface hydroxy to form a hydroxy radical.

$\nu_{as}(OCO)$ and the bending vibration of C–H (δ(CH)) at 2970 cm^{-1}, the stretching vibration of C–H (ν(CH)) at 2880 cm^{-1}, the coupling mode of ν_s(OCO) and δ(CH) at 2740 cm^{-1}, and δ(CH) at 1383 cm^{-1} [43,44]. For Cu–spheroidal ZnO, the peaks at 1630 cm^{-1} and 1339 cm^{-1} were observed at 46 Pa of CO and can be assigned to ν_{as}(OCO) and ν_s(OCO) peaks of the formate species, respectively (Scheme 1A–b). Furthermore, under these conditions or at 46 Pa of CO and 46 Pa of O_2 under UV–visible light, peaks at 2985 cm^{-1} and 2879 cm^{-1} were observed due to ν_{as}(OCO) + δ(CH) and ν(CH), respectively. The five peaks (2985, 2879, 1627, 1587, and 1297 cm^{-1}) under CO + O_2 illuminated with UV–visible light were well compared to five peaks (2952, 2877, 1645, 1620, and 1320 cm^{-1}) given at 46 Pa of formic acid for Cu–spheroidal ZnO sample. The peak due to ν_s(OCO) + δ(CH) was not clearly resolved because of the low signal/background ratio.

For Cu–spheroidal ZnO, the adsorbed Cu ions clearly exhibited a promoting effect to enhance CO_2 formation by a factor of 3.3 (Fig. 6A, C) and therefore should be incorporated in the promoted photo-PROX reaction mechanism. The redox potential values for the Cu ions and the reaction steps in the photo-PROX reaction are as follows:

$$Cu^{2+} + e^- \rightleftarrows Cu^+, \; E^o = 0.159 \; V$$

$$O_2 + 2H^+ + 2e^- \rightarrow H_2O_2, \; E^o = 0.695 \; V$$

$$HCO_2H \rightarrow CO_2 + 2H^+ + 2e^-, E^o = -0.199 \; V$$
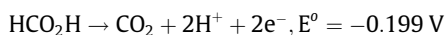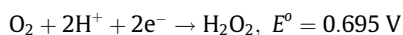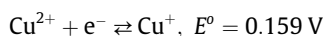
We propose that the electrons produced in ZnO under UV–visible light diffused to Cu^{II} sites on the surface, especially effectively for shorter spheroidal ZnO (35.1 nm in average) than for longer rod-like ZnO (443 nm in average) before they recombined with holes during the diffusion, and the trapped electrons as Cu^I state were transferred to O_2 (Scheme 1A–c). The energetic is depicted in Scheme 2 including the electron flow from valence band to conduction band, to Cu ions (or directly from VB to Cu ions), and then to O_2 species. Based on the comparison of the reduction potential values, steps b to c can not only be considered as the diffusion of photogenerated electrons to Cu^{II} sites and holes to the formate species but also as the electron transfer from formate to Cu^{II}. Route A assumes effective H$^+$ transfer from the formate species to the neighboring reduced O_2-derived species on the Cu ion sites.

On the other hand, Route B assumes H$^+$ transfer from the surface hydroxy species to the reduced O_2-derived species on the Cu sites (Scheme 1B–c → d). A shoulder peak at 3666 cm^{-1} and a broad peak centered at 3310 cm^{-1} were observed for as-prepared Cu–spheroidal ZnO and are assigned to isolated hydroxy and hydrogen-bonded hydroxy species, respectively. In both Routes A and B, hydroxy radicals are formed by the photoreduction of O_2 and promote the decomposition of formates (Scheme 1Af → b)
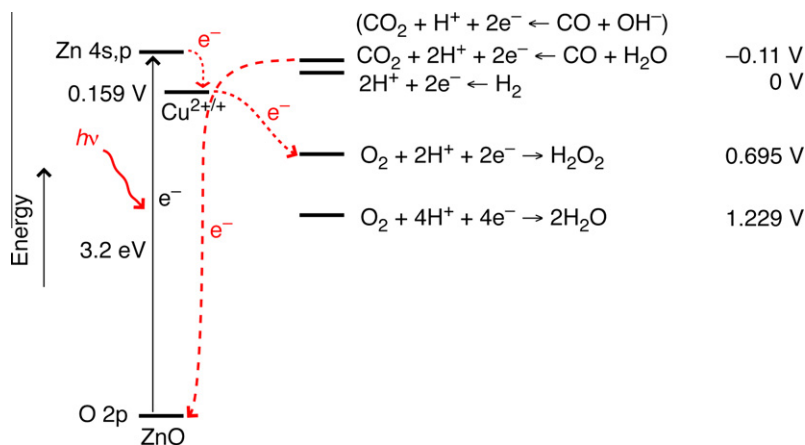
Scheme 2. Energy levels at the bandgap of ZnO and $Cu^{2+/+}$ ions versus the reaction steps of photo-PROX of CO.

[45] or directly react with CO to form CO_2 and H^+ (Scheme 1Bg → a).

In both Routes A and B, if hydrogen peroxide was reduced through coupling with H^+, water was produced as a byproduct. In the photo-PROX reactions, the initial CO_2 formation rates decreased from 94 µmol h^{-1} g_{cat}^{-1} in the absence of H_2 to 18 µmol h^{-1} g_{cat}^{-1} under 63 kPa of H_2 (Table 2D–H). In contrast, water formation rates were nearly constant between 2.9 µmol h^{-1} g_{cat}^{-1} and 4.3 µmol h^{-1} g_{cat}^{-1} under these photocatalytic reaction conditions. Hydrogen did not simply affect the CO oxidation reaction by enhancing the by-reaction to form water. Instead, it inhibited the adsorption sites of CO, for example, by the decomposition of formates (Scheme 1A–b).

5. Conclusions

In this study, spheroidal and rod-like ZnO semiconductors were synthesized. Based on the XRD peak intensity ratio and SEM and high-resolution TEM images, both samples were found to preferentially and anisotropically grow in the c-axis direction (22 nm × 47 nm and 80 nm × 443 nm, respectively). The specific surface area of spheroidal ZnO (35 m^2 g^{-1}) was 1.75 times greater than that of rod-like ZnO, and their semiconductivity was similar (E_g = 3.21 eV). However, the initial CO_2 formation rate in the photo-PROX of CO using spheroidal ZnO (17 µmol h^{-1} g_{cat}^{-1}) was 40.5 times greater than that using rod-like ZnO, strongly suggesting critically dependent photocatalytic activity on the exposed crystal face and effective electron/hole diffusion length to each crystal face before charge recombination takes place.

The adsorption of 0.5 wt.% of Cu^{2+} ions was found to be effective for promoting and tuning the photo-PROX reactivity of CO using spheroidal ZnO. The initial CO_2 formation rate using Cu–spheroidal ZnO was further increased by a factor of 3.3 compared with that for spheroidal ZnO. When the initial pressures were 63 Pa of CO, 150 Pa of O_2, and 6.3 kPa of H_2, CO was decreased to 0.35 ppm in 5 h under UV–visible light. The comparison of photo-PROX performance under visible light indicated that photoreactivity was mostly due to UV light illumination (<420 nm).

The photogenerated electron trap at the Cu^{II} sites was demonstrated as the increase in the shoulder peak at 8983.1 eV, specifically for Cu^I sites below the Cu K-absorption edge. Under photo-PROX reaction conditions, the increase in the rate was 4.1 µmol h^{-1} g_{cat}^{-1} and 15.6% of Cu sites were reduced to Cu^I in 3 h. In the FT-IR spectra under photo-PROX reaction conditions, the peaks due to the hydroxy group were observed at 3666 cm^{-1} and 3310 cm^{-1} and the peaks due formate species were observed at 2985 cm^{-1}, 2879 cm^{-1}, 1627 cm^{-1}, 1587 cm^{-1}, and 1297 cm^{-1}.

The reaction of CO with the hydroxy group produced formate species, and the O_2-derived species would be reduced by the Cu^I sites and would accept protons from the neighboring formate species.

References

[1] L. Schlapbach, Nature 460 (2009) 809.
[2] H.A. Gasteiger, N.M. Marković, Science 324 (2009) 48.
[3] F. Rouquerol, J. Rouquerol, K. Sing, Adsorption by Powders and Porous Solids – Principles, Methodology, and Applications, London, 1999, p. 357.
[4] Y.M. Lin, M.H. Rei, Sep. Purif. Technol. 25 (2001) 87.
[5] A. Cho, Science 299 (2003) 1684.
[6] A.T. Bell, Science 299 (2003) 1688.
[7] A. Fukuoka, J. Kimura, T. Oshio, Y. Sakamoto, M. Ichikawa, J. Am. Chem. Soc. 129 (2007) 10120.
[8] G.R. Bamwenda, S. Tsubota, T. Nakamura, M. Haruta, Catal. Lett. 44 (1997) 83.
[9] T. Kamegawa, T.H. Kim, J. Morishima, M. Matsuoka, M. Anpo, Catal. Lett. 129 (2009) 7.
[10] T. Kamegawa, R. Takeuchi, M. Matsuoka, M. Anpo, Catal. Today 111 (2006) 248.
[11] X.L. Zhang, Y.H. Kim, Y.S. Kang, Curr. Appl. Phys. 6 (2006) 796.
[12] T. Kawano, H. Imai, Cryst. Growth Des. 6 (2006) 1054.
[13] Y. Izumi, D. Obaid, K. Konishi, D. Masih, M. Takagaki, Y. Terada, H. Tanida, T. Uruga, Inorg. Chim. Acta 361 (2008) 1149.
[14] R. Zanella, S. Giorgio, C.R. Henry, C. Louis, J. Phys. Chem. B 106 (2002) 7634.
[15] Y. Izumi, T. Itoi, S. Peng, K. Oka, Y. Shibata, J. Phys. Chem. C 113 (2009) 6706.
[16] X. Gao, I.E. Wachs, J. Phys. Chem. B 104 (2000) 1261.
[17] J.A. Bearden, Rev. Mod. Phys. 39 (1967) 78.
[18] G. Zschornack, Handbook of X-ray Data, Springer, Berlin/Heidelberg, 2007. p. 233.
[19] M. Vaarkamp, H. Linders, D. Koningsberger, XDAP Version 2.2.7, XAFS Services International, Woudenberg, The Netherlands, 2006.
[20] N. Ahmed, Y. Shibata, T. Taniguchi, Y. Izumi, J. Catal. 279 (2011) 123.
[21] N. Ahmed, M. Morikawa, Y. Izumi, Catal. Today, doi:10.1016/j.cattod.2011.08.010.
[22] Y. Izumi, K. Konishi, H. Yoshitake, Bull. Chem. Soc. Jpn. 81 (2008) 1241.
[23] B.G. Hyde, S. Andersson, Inorganic Crystal Structures, John Wiley & Sons, New York, 1989. p. 55.
[24] P.K. Giri, S. Bhattacharyya, D.K. Singh, R. Kesavamoorthy, B.K. Panigrahi, K.G.M. Nair, J. Appl. Phys. 102 (2007) 093515.
[25] A.J. Reddy, M.K. Kokila, H. Nagabhushana, R.P.S. Chakradhar, C. Shivakumara, J.L. Rao, B.M. Nagabhyshana, J. Alloys Compds. 509 (2011) 5349.
[26] I.J. Pickering, G.N. George, Inorg. Chem. 34 (1995) 3142.
[27] E.I. Solomon, P.M. Jones, J.A. May, Chem. Rev. 93 (1993) 2623.

[28] Y. Izumi, H. Nagamori, Bull. Chem. Soc. Jpn. 73 (2000) 1581.
[29] L.S. Kau, J. Spira-Solomon, J.E. Penner-Hahn, K.O. Hodgson, E.I. Solomon, J. Am. Chem. Soc. 109 (1987) 6433.
[30] T.J. Whang, M.T. Hsieh, J.M. Tsai, S.J. Lee, Appl. Surf. Sci. 257 (2011) 9539.
[31] S. Li, J.L. Li, Q. Jiang, G.W. Yang, J. Appl. Phys. 108 (2010) 024302.
[32] B. Schumacher, Y. Denkwitz, V. Plazak, M. Kinne, R.J. Behm, J. Catal. 224 (2004) 449.
[33] E. Moretti, L. Storaro, A. Talon, P. Patrono, F. Pinzari, T. Montanari, G. Ramis, M. Lenarda, Appl. Catal. A 344 (2008) 165.
[34] D. Beydoun, H. Tse, R. Amal, G. Low, S. McEvoy, J. Mol. Catal. A 177 (2002) 265.
[35] O.K. Varghese, M. Paulose, T.J. LaTempa, C.A. Grimes, Nano Lett. 9 (2009) 731.
[36] O. Lopatiuk, L. Chernyak, Appl. Phys. Lett. 87 (2005) 162103.
[37] A. Soudi, P. Dhakal, Y. Gu, Appl. Phys. Lett. 96 (2005) 253115.
[38] K. Park, J. Xi, Q. Zhang, G. Cao, J. Phys. Chem. C 115 (2011) 20992.
[39] I. Schmitt, K. Fink, V. Staemmler, Phys. Chem. Chem. Phys. 11 (2009) 11196.
[40] I.X. Green, W. Tang, M. Neurock, J.T. Yates Jr, Science 333 (2011) 736.
[41] S.K. Youn, N. Ramgir, C. Wang, K. Subannajui, V. Cimalla, M. Zacharias, J. Phys. Chem. C 114 (2010) 10092.
[42] X. Xie, Z.Q. Liu, M. Haruta, W. Shen, Nature 458 (2009) 746.
[43] S. Fujita, M. Usui, H. Ito, N. Takezawa, J. Catal. 157 (1995) 403.
[44] G. Busca, J. Lamotte, J.C. Lavalley, V. Lorenzelli, J. Am. Chem. Soc. 109 (1987) 5197.
[45] G.R. Dey, K.N.R. Nair, K.K. Pushpa, J. Nat. Gas Chem. 18 (2009) 50.